

MEASURING POLARIZATION WITH DASI

E. M. LEITCH, J. M. KOVAC, C. PRYKE, B. REDDALL, E. S. SANDBERG, M. DRAGOVAN¹ AND J. E. CARLSTROM

University of Chicago, Department of Astronomy & Astrophysics, Department of Physics, Enrico Fermi Institute, 5640 South Ellis Avenue, Chicago, IL 60637

AND

N. W. HALVERSON AND W. L. HOLZAPFEL

University of California, Department of Physics, Le Conte Hall, Berkeley, CA 94720

Submitted to the Astrophysical Journal

ABSTRACT

We describe an experiment to measure the polarization of the Cosmic Microwave Background (CMB) with the Degree Angular Scale Interferometer (DASI), a compact microwave interferometer optimized to detect CMB anisotropy at multipoles $l \simeq 140 - 900$. The telescope has operated at the Amundsen-Scott South Pole research station since 2000 January. The telescope was retrofit as a polarimeter during the 2000 - 2001 austral summer, and throughout the 2001 and 2002 austral winters has made observations of the CMB with sensitivity to all four Stokes parameters. The telescope performance has been extensively characterized through observations of artificial sources, the Moon, and polarized and unpolarized Galactic sources. In 271 days of observation, DASI has differenced the CMB fluctuations in two fields to an rms noise level of $2.8 \mu\text{K}$.

1. INTRODUCTION

The DASI experiment, previously described in Leitch et al. (2002) (hereafter Paper I), is an interferometric array designed to measure anisotropy in the cosmic microwave background radiation. The telescope was deployed to the Amundsen-Scott South Pole Station in the 1999 - 2000 austral summer and made total intensity measurements of the CMB during the 2000 austral winter. These observations were described in Paper I. The angular power spectrum of the CMB derived from these data were reported by Halverson et al. (2002) (hereafter Paper II) and the constraints on cosmological parameters derived from the power spectrum were presented by Pryke et al. (2002) (hereafter Paper III).

During the 2000 - 2001 austral summer, the DASI receivers were each fitted with broadband achromatic polarizers to allow polarization-sensitive observations of the CMB. In addition, a large reflecting ground screen was installed to reduce the sensitivity to terrestrial sources of emission. Throughout the 2001 and 2002 austral winters, the telescope has observed the CMB in all four Stokes parameters. This paper (Paper IV in the continuing series) describes the design of the DASI CMB polarization experiment, the polarization response and calibration of the instrument, and the CMB observations made during the 2001 and 2002 seasons. The analysis of the CMB polarization data obtained is presented by Kovac et al. (2002) (hereafter Paper V).

2. MEASURING POLARIZATION WITH DASI

The DASI telescope has been extensively described in Paper I. Here we describe only hardware that has been modified or added since the observations discussed in that paper, and briefly recapitulate details pertinent to understanding the polarization response of the array.

DASI consists of an array of thirteen lensed, corrugated

feed horns, 20 cm in diameter, each surrounded by a corrugated shroud to suppress cross-talk between the horns. The array operates in 10 1-GHz bands over the frequency range 26 - 36 GHz, with horn separations ranging from 25.1 - 120.73 cm, sampling points in the Fourier (u, v) plane at radii of 22 - 143 λ^{-1} , or equivalently, multipoles in the range $l \simeq 140 - 900$ at the frequency extrema.

The feed horns are distributed in a three-fold symmetric pattern on a rigid faceplate which can be rotated about its axis to observe at a range of parallactic angles. The entire faceplate is in turn attached to an altitude-azimuth mount. DASI is thus a co-planar array and the projected baselines do not change as a source is tracked around the sky. Given the symmetry of the array, rotations of the faceplate which are integral multiples of 60° produce identical Fourier-space sampling.

2.1. Receiver Polarization Hardware

The first stage of each DASI receiver is a single-moded, i.e., a single polarization state, HEMT amplifier. DASI does not use orthomode transformers to separate orthogonal polarization states. Instead, a mechanically switchable waveguide polarizer is inserted between the amplifier and the feedhorn to select between left- and right-handed polarization states, L and R .

The DASI horns feed circular waveguide, which by its symmetry is dual moded. The circular waveguide is gradually tapered to single-mode rectangular waveguide which passes only one mode of linear polarization. For sensitivity to circular polarization, a transformation from circular to linear polarization must therefore be made in the circular waveguide or outside of the feed. The standard technique uses a $\lambda/4$ retarder oriented 45° to the E -field of the linear polarization accepted by the rectangular waveguide. This retarder is usually a simple dielectric vane inserted

¹ Current address: Jet Propulsion Laboratory, California Institute of Technology, 4800 Oak Grove Drive, Pasadena, CA 91109

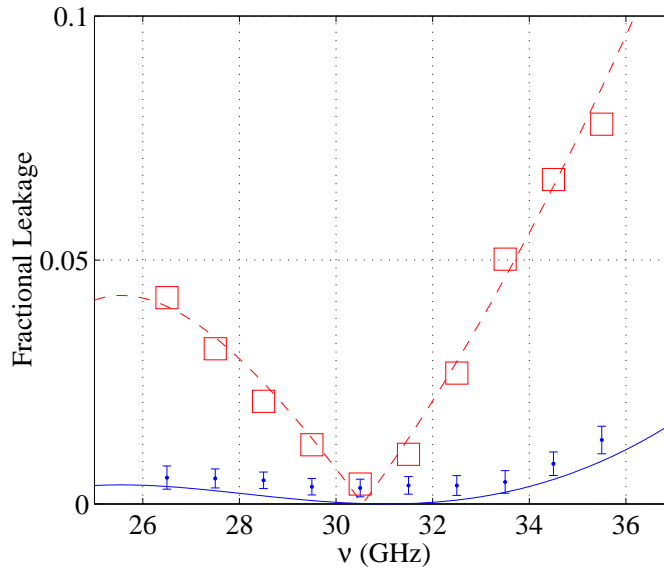


FIG. 1.— Theoretical minimum instrumental polarization for a single-element polarizer (dashed line), and for a 2-element polarizer (solid line). Squares are benchtop measurements of a single-element polarizer. Points are the astronomical measurements of the average on-axis instrumental polarization for the 13 DASI receivers configured with 2-element polarizers.

in the circular waveguide; at 30 GHz, the loss in the dielectric and the associated noise added to the system are negligible if the vane is cooled. The circular waveguide which holds the vane can be mechanically rotated along the waveguide axis by $\pm 45^\circ$ to select L or R .

DASI uses a mechanically-switched circular waveguide dielectric polarizer similar to that outlined above. However, a simple $\lambda/4$ retarder leads to a contribution from the unwanted circular polarization state, referred to as *leakage*, which is a function of the offset from the design frequency. Due to DASI's large fractional bandwidth, the leakage for a simple $\lambda/4$ retarder polarizer would be prohibitively large at the band edges (see Figure 1).

To construct broadband, low-leakage polarizers, we investigated designs using multiple retarder elements and found that there are solutions to meet any specified polarization purity and bandwidth. For more details of the theory of multi-element achromatic waveguide polarizers and for details of the DASI polarizers, including extensive laboratory test results, see Kovac & Carlstrom (2002). For the DASI polarizers we selected a two element design composed of $\lambda/2$ and $\lambda/4$ dielectric retarding waveguide vanes made from 1.3 mm thick polystyrene. With a two element design, the retarders can be arranged so that the offset-frequency errors cancel to first order. The design also incorporates an absorbing vane to suppress the linear polarized mode that is reflected by the circular to rectangular waveguide transition.

To aid in understanding the DASI design, consider the signal path as if the receivers were actually transmitters starting with linear polarization in the rectangular waveguide which the polarizer then transforms to circular polarization. In the DASI design, the $\lambda/2$ retarder then simply introduces a rotation of the E -field of the linear polarization at the design frequency, but also introduces an offset frequency error due to the dispersion across the band. The

$\lambda/4$ retarder is oriented 45° to the rotated E -field to produce the desired circular polarization. The orientation of the $\lambda/2$ retarder to the incident polarization is chosen such that dispersion effects of the two retarders cancel to first order. The entire assembly is then mechanically rotated to select L or R polarization. The offset angle between the $\lambda/2$ and $\lambda/4$ retarders is held fixed at 60° . The angles of the $\lambda/2$ retarder to the E -field of the linear polarization to produce the orthogonal circular polarization states are 15° and 105° . In Figure 1, we show the predicted leakage for the DASI 2-element design and, for comparison, the traditional single $\lambda/4$ design. Also shown in Figure 1 is the leakage response determined from astronomical observations, as discussed in §2.7.1.

The stability of the polarization leakages is more critical than their magnitude since the leakages, if stable, can be corrected for in the data analysis. For DASI the stability of the polarizers is set by the repeatability and accuracy with which the angle is set. The polarizers are driven by a stepper motor with a $0^\circ:9$ half-step, geared down by a factor of three using anti-backlash gears, to provide $0^\circ:30$ steps of the vane assembly. The position of the polarizer is read by an encoder with $0^\circ:12$ steps. All of the hardware is contained under vacuum within the receiver cryostats. The motor and encoder are warm, but the waveguide vane assembly is cooled to ~ 10 K. With 2.5 counts of the polarizer encoder for the minimum step of the motor, we can ensure a repeatable return to the same position. We have verified that the stepper motor holds the polarizer position to better than half of an encoder count ($< 0^\circ:06$) for the entire season. This accuracy translates to a variation in the leakage of less than 0.1%. Astronomical tests of the stability of the leakages on long time scales are given in §2.7.1.

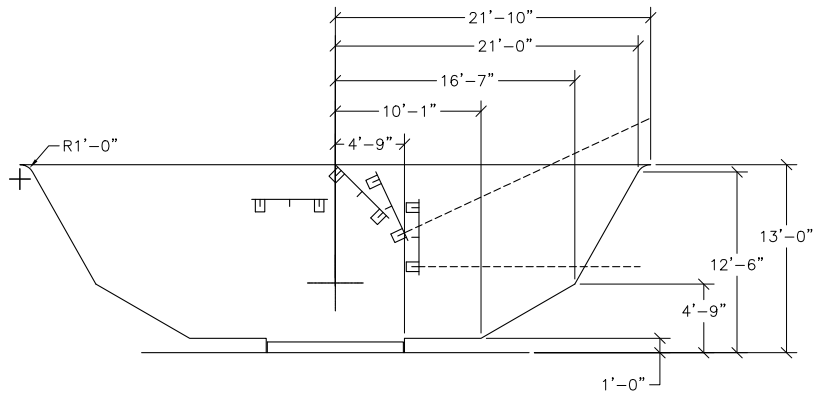


FIG. 2.— Ground shield geometry. The ground shields are designed to reflect sidelobes of the horns to the cold sky, and to prevent sidelobes from seeing other horns, due to concerns about crosstalk.

A ground shield was installed around the telescope during the 2000 – 2001 austral summer, and was in place for the entirety of the 2001 – 2002 observations presented here. The ground shield is designed to reflect the antenna sidelobes onto the cold sky, and consists of three concentric rings of twelve panels, the innermost flat, the outer two rising at a pitch which increases from $\sim 36^\circ$ for the inner ring to $\sim 60^\circ$ for the outer (see Figure 2). The design of the panels was guided by concerns about crosstalk between close-packed array elements; panels are configured to prevent sidelobes up to 90° off-axis from seeing any other horns in reflection.

The top of the outermost ring extends to a height of 13 feet above the roofline. The uppermost border of the shield is rolled with a 1 foot radius to reduce diffraction around the edge, and all gaps between panels are covered with aluminum adhesive tape. Four of the upper panels are hinged and may be lowered to allow observations of planets, or a test transmitter mounted on the roof of one of the station buildings. Without lowering the shields, the minimum observing elevation is $\sim 25^\circ$.

Although the DASI telescope was intended to operate with the ground shield from its inception, the shield panels were not in place during the year-2000 observations reported in Papers I and II, and considerable effort was devoted to reducing the effect of the residual ground signal in that data set. Throughout those observations, the effect of the ground was easily visible in the raw data and is a strong function of (u, v) radius.

During both 2000 and 2001, fields were observed in consecutive 1-hour blocks over the same azimuth range (see §4), and we can probe for residual contamination from the ground by forming the difference between successive 1-hour means. In the 2000 data, taken without the ground shield, comparison of the variance in these 2-hour differences to the variance in data differenced at the 8-second integration rate indicates a significant (5%) noise excess, dominated by the data on the shortest baselines. In the 2001 co-polar data, taken with the ground shield in place, the noise excess has dropped by nearly an order of magnitude. Any noise excess in the cross-polar data is a factor of 3 – 4 lower still, indicating that any residual signal from

the ground is largely unpolarized.

2.3. Sun Shield

When the Sun is above the horizon, data taken over much of the sky is contaminated by signal entering the far-off sidelobes of the horn beam pattern. This is most evident as long-period fringing in visibility data taken within $\sim 60^\circ$ of the Sun (for a definition of visibility, see §2.4). Although sunset and sunrise at the pole occur at the March and September equinoxes, the station is typically closed due to the excessive cold from the middle of February until the last week in October, resulting in approximately three months of time during which the telescope is inaccessible but the data are unusable for CMB observations.

To extend the effective observing season, a sunshield was constructed during the austral summer of 2001 – 2002, and was in place throughout the 2002 observations. The lightweight conical shield, constructed from the top ~ 3 feet of a spare shield from the TopHat experiment, attaches rigidly to the front face of the telescope, completely enclosing, but not rotating with, the faceplate. With a diameter at the attachment point of $62.93''$, and an opening angle of 15° , the shield prevents any sidelobe of an antenna from seeing the Sun when the telescope is pointed $> 65^\circ$ away.

Contamination from the Sun was plainly evident in the 2000 data as fringing in the calibrator visibility data taken after sunrise, and is evident as increased scatter on the shortest baselines even in the 2001 data taken with the ground shield present. These data show excursions in the visibility amplitude on the shortest baselines of $\sim 50\%$ about the pre-sunrise means, although the longest baselines are unaffected. In data taken during the 2002 sunset with the sunshield present, there is still some evidence for increased scatter in the short-baseline visibilities, but the effect is reduced by nearly two orders of magnitude. For fields $> 90^\circ$ from the Sun, the visibility scatter is consistent with the noise on all baseline lengths.

The sunshield was left in place throughout the 2002 winter season, and it is found that during periods when the Moon is above the horizon but below 10° elevation, the data from 2002 show evidence of excess noise, while the

2001 data do not. We speculate that during periods when the Moon is within the opening angle of the sunshield, secondary reflection off the shield can actually contaminate the short-baseline data when the Moon would otherwise be screened by the ground shield. Accordingly, a stricter cut on the Moon elevation is applied to the 2002 data than to the 2001 data (see §4.3.2).

2.4. Polarization Response

To derive the polarization response of an interferometer, consider the complex electric field incident on a single receiver, E_m . The response of the interferometer on a baseline m - n , called the *visibility*, is simply the time-averaged cross-correlation of the fields from a pair of receivers (m, n):

$$V_{mn} = \langle E_m E_n^* \rangle. \quad (1)$$

Rewriting E_m in terms of its components in an arbitrary coordinate system rotated by an angle ψ relative to a coordinate system fixed to the receivers (i.e., parallactic angle), the usual Stokes parameters can be substituted to obtain

$$\begin{aligned} V_{mn}^{RR} &= \frac{1}{2} \{S_I + S_V\} \\ V_{mn}^{LL} &= \frac{1}{2} \{S_I - S_V\} \\ V_{mn}^{RL} &= \frac{1}{2} \{S_Q + iS_U\} e^{-2i\psi} \\ V_{mn}^{LR} &= \frac{1}{2} \{S_Q - iS_U\} e^{2i\psi} \end{aligned} \quad (2)$$

for receivers set to receive right circular (R) and left circular (L) polarization. We refer to these four combinations as *Stokes states*, by analogy with the Stokes parameters which can be derived from them.

Since the DASI correlator was originally designed to accommodate only a single Stokes state per IF, observation in all four states is achieved via time-multiplexing. The polarizer for each receiver is switched between L and R on a Walsh sequence which spends an equal amount of time in each state, i.e., $\sum_i f_i = 0$ if we represent the two states as $f \in \pm 1$. The product of two Walsh functions is another Walsh function, whence $\sum_{i,n \neq m} f_i^n f_i^m = 0$, and the baseline therefore spends an equal amount of time in the co-polar (RR, LL) and cross-polar (LR, RL) states. In fact, it can be shown that with this sequencing of the polarizers, over the course of a full Walsh cycle each baseline of the interferometer spends an equal amount of time in each of the four Stokes states, although different baselines will sample different Stokes states at any given time. For the observations presented here, a Walsh function of period 16 with a time step of 200 seconds was used, so that over the course of an hour, every Stokes state is sampled by every baseline for approximately 13 minutes.

2.5. Relative Gain and Phase Calibration

In practice, each receiver introduces a unique phase offset and amplitude variation to the electric field, so that the expression for the detected field must be modified by a receiver-dependent complex gain, $\tilde{E}_m = g_m E_m$, where g_m depends on the polarization state of the receiver. Furthermore, the correlator can introduce baseline-dependent

complex gains g_{mn} , independent of polarization state, so that the measured visibilities are given by:

$$\begin{aligned} \tilde{V}_{mn}^{RR} &= g_m^R g_n^{R*} g_{mn} V_{mn}^{RR} \equiv G_{mn}^{RR} V_{mn}^{RR} \\ \tilde{V}_{mn}^{LL} &= g_m^L g_n^{L*} g_{mn} V_{mn}^{LL} \equiv G_{mn}^{LL} V_{mn}^{LL} \\ \tilde{V}_{mn}^{RL} &= g_m^R g_n^{L*} g_{mn} V_{mn}^{RL} \equiv G_{mn}^{RL} V_{mn}^{RL} \\ \tilde{V}_{mn}^{LR} &= g_m^L g_n^{R*} g_{mn} V_{mn}^{LR} \equiv G_{mn}^{LR} V_{mn}^{LR}. \end{aligned} \quad (3)$$

Since the co-polar visibilities V_{mn}^{RR} and V_{mn}^{LL} are just proportional to Stokes $S_I \pm S_V$, the gain factors G_{mn}^{RR} and G_{mn}^{LL} can simply be derived on a per-baseline basis from observations of a bright unpolarized point source, or more complicated source whose intrinsic visibility structure is known (if we take the circular polarization S_V to be zero).

However, we require a source of known linear polarization to derive the complex gains in the same manner for the cross-polar visibilities \tilde{V}_{mn}^{RL} and \tilde{V}_{mn}^{LR} . These are in general scarce at high frequencies, and furthermore few are well studied in the southern hemisphere. The low gain of DASI's 20-cm feed horns, moreover, makes it impracticable to observe all but the brightest sources, in total intensity or otherwise, and the brightest sources at 30 GHz are typically compact HII regions, whose polarization fraction is expected to be negligible.

As can be seen from Equation 3, however, we can in principle derive the cross-polar gains from co-polar observations of an unpolarized source, if we work in ratios of complex gains:

$$\frac{\tilde{V}_{mn}^{LL}}{\tilde{V}_{mn}^{RR}} = \left(\frac{g^L}{g^R}\right)_m \left(\frac{g^L}{g^R}\right)_n^* \equiv r_m r_n^* \quad (4)$$

in which the correlator gains g_{mn} exactly cancel. For DASI, this yields an overconstrained set of 78 complex equations which can be solved for the 13 antenna-based ratios $r_k = g_k^L/g_k^R$.

The solution is not unique, and we must arbitrarily specify the phase $\Delta\phi \equiv \phi_R - \phi_L$ of one of the ratios, typically setting it to zero. With the ratios r_k in hand, the baseline complex gains for the cross-polarized channels can be recovered from the co-polar solutions as:

$$\begin{aligned} r_n^* G_{mn}^{RR} &= \left(\frac{g^L}{g^R}\right)_n^* g_m^R g_n^{R*} g_{mn} = e^{-i\Delta\phi} G_{mn}^{RL} \\ r_m G_{mn}^{RR} &= \left(\frac{g^L}{g^R}\right)_m g_m^R g_n^{R*} g_{mn} = e^{i\Delta\phi} G_{mn}^{LR} \end{aligned} \quad (5)$$

that is, we can construct the cross-mode calibration factors from the antenna-based solutions, but only up to the unknown phase difference between R and L for our reference antenna. This overall phase offset, while leaving the amplitude of the cross-polar visibilities unaffected, will mix power between S_Q and S_U , or between E and B , in terms of the decomposition into the coordinate-independent scalar fields which has become the standard in the CMB polarization literature (Kamionkowski, Kosowsky, & Stebbins 1997; Zaldarriaga & Seljak 1997; Hu & White 1997). Removal of the offset is therefore critical to obtaining a clean separation of CMB power into E - and B -modes.

In practice, we use the bright, compact, unpolarized HII region, RCW38, to determine the co-polar and cross-polar calibration factors in this manner. The phase offset can only be determined by observing a source whose plane of polarization is known, as described in the next section.

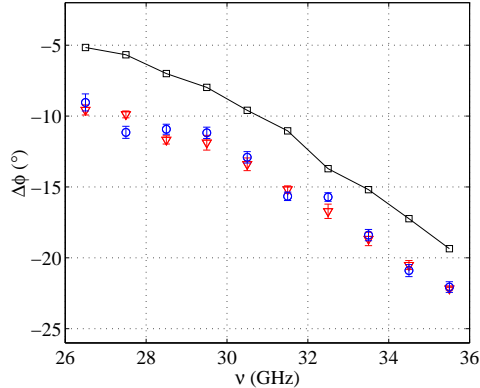


FIG. 3.— The absolute phase offsets determined from wire grid observations (triangles) and from the Moon (circles). Shown also are benchtop measurements of the same polarizer (solid line, squares), with an arbitrary offset subtracted.

2.6. Absolute Phase Calibration

To determine the phase offset introduced by the complex gain correction described above, we require a source whose polarization angle (though not amplitude) is known. As discussed in §2.5, however, few suitably strong polarized sources are available, and in practice we create a source of known polarization angle by observing an unpolarized source through polarizing wire grids. At centimeter wavelengths, the required wire spacing ($\lesssim \lambda/3$) poses no particular technical challenges, and grids can be simply constructed out of conventional materials; thirteen wire grids were constructed out of 34-gauge copper wire, wound with a spacing of $0.05''$. These grids attach directly to the exterior of the corrugated shrouds and completely cover the aperture of the DASI horns.

The same source used for gain calibration of the visibilities, RCW38, was observed with the wire grids attached in two orientations, one with wires parallel to the ground, and the other with grids (but not receivers) rotated by 45 degrees with respect to the first. It was confirmed that in the second orientation the apparent phase of the cross-polar visibilities shifted by $\pm 90^\circ$ relative to the first, as indicated by Equation 2.

The measured absolute phase offsets $\Delta\phi(\nu)$ are shown in Figure 3. These offsets show a trend in frequency which is a direct consequence of the achromatic polarizer design discussed in §2.1. As Figure 3 shows, this trend is in excellent agreement with expectations from benchtop measurements of the polarizers, where the expected trend is shown with an arbitrary offset subtracted. These phase offsets were measured in 2001 August and again in 2002 February and were found to agree within measurement errors. As discussed below, we can restrict the intrinsic polarization fraction of RCW38 to $< 0.09\%$ at our observing frequency; since the grids create a polarized source with an effective polarization fraction of 100%, any intrinsic polarized flux at this level will have a negligible effect on the measurements of the absolute phase offsets.

Although suitably bright point sources of known polarization angle are not available, we can in principle derive the absolute phase offsets from observations of the Moon, as discussed in §3.1. These results, also shown in Figure 3, are consistent with the offsets measured with the wire grid polarizers, to within the ~ 0.4 measurement errors. As

discussed in Paper V, errors in the absolute phase offset of this magnitude have a negligible effect on the power spectral analysis.

2.7. Instrumental Polarization

For perfect polarizers, circular polarization can be thought of as the superposition of two orthogonal linear modes, $E = \alpha E_x + \beta E_y$, where one mode leads the other by exactly 90° , i.e., $\beta/\alpha = e^{\pm i\pi/2}$. For perfect polarizers, the cross-polar visibilities are strictly linear combinations of the linear polarization measures, Stokes S_Q and S_U , as indicated by Equation 2. For realistic polarizers, however, a small amount of radiation of one handedness will be passed by a polarizer set to transmit the opposite handedness, leading to a term in the expression for the cross-polar visibilities proportional to the total intensity. In the limit of small deviations from perfect orthogonality, $\beta/\alpha \simeq i(1 - \epsilon)$, and keeping only terms to first order in ϵ , it can be shown that the cross-polar visibilities are given by:

$$\begin{aligned} V_{mn}^{RL} &= \frac{1}{2} \left\{ (S_Q + iS_U)e^{-2i\psi} + S_I(\epsilon_m^R + \epsilon_n^{L*}) \right\} \\ V_{mn}^{LR} &= \frac{1}{2} \left\{ (S_Q - iS_U)e^{2i\psi} + S_I(\epsilon_m^L + \epsilon_n^{R*}) \right\} \end{aligned} \quad (6)$$

The terms $L^{RL} \equiv \epsilon_m^R + \epsilon_n^{L*}$ and $L^{LR} \equiv \epsilon_m^L + \epsilon_n^{R*}$ are sums of the polarizer leakages discussed in §2.1, and are expected from benchtop measurements of the DASI polarizers to be on average $< 1\%$ (see Figure 1). As is obvious from Equation 6, the presence of leakages has the effect of mixing S_I into S_Q and S_U , or equivalently, the leakages will mix CMB power from T into E and B (see also Paper V).

2.7.1. On-Axis Leakage

As discussed in §2, the receivers are mounted on a rigid faceplate which can be driven to simulate parallactic angle rotation. From Equation 6, it can be seen that the leakages are irrotational, while any contribution to the visibilities from intrinsic source polarization will have a phase modulated by the faceplate rotation. The data can therefore be fit for an offset plus a sinusoidal modulation to isolate the leakages. Equivalently, when observations are made at three or six-fold symmetric faceplate rotations, the cross-polar visibilities for a radially symmetric source can simply

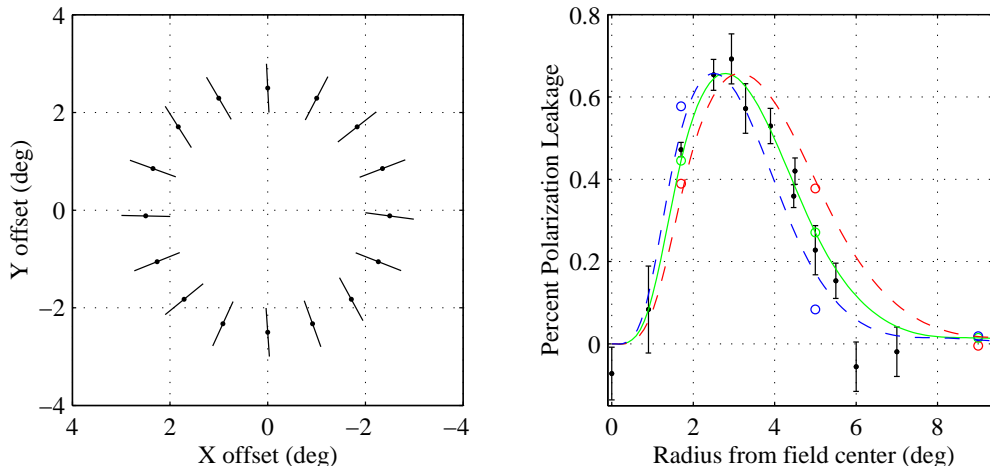


FIG. 4.— (left) The measured direction of the instrumental leakage for a ring of 2.5° offset pointings on RCW38. (right) The amplitude profile of the instrumental polarization shown versus radius from field center. Moon data are shown as red, green and blue circles corresponding to the frequency bands 26 – 29, 29 – 33, and 33 – 36 GHz respectively. RCW38 data for the full 26 – 36 GHz band are shown as black points. The green line is a spline interpolation of the 29 – 33 GHz Moon data, and the red and blue dashed lines are the interpolation scaled to 27.5 and 34.5 GHz respectively. See text for further discussion.

be averaged over faceplate rotations to cancel the intrinsic term.

To determine the magnitude of the leakages, RCW38 was observed at six faceplate rotations separated by 60° , for approximately 3 hours at each faceplate position, resulting in an rms noise on the baseline leakages of 0.8% (of S_I). As can be seen from Equation 6, however, the baseline leakages are simply linear combinations of antenna-based terms, and can therefore be solved for the antenna-based leakages ϵ , yielding a typical error of 0.3% on the antenna-based leakages. Typical antenna-based leakage amplitudes range from $\lesssim 1\%$ over much of the frequency band, to $\sim 2\%$ at the highest frequency. The averages of the antenna-based leakages $\epsilon^{R,L}$ are shown in Figure 1. Prior to installation on the telescope, the polarizers were optimized in a test setup to minimize the leakage response; as can be seen in Figure 1, these observations indicate that we have achieved close to the theoretical minimum. As discussed in Paper V, leakages of this magnitude have a negligible effect on the separation of the CMB signal into E and B modes.

Of critical importance is the stability of the leakages, as they cannot be frequently measured. The leakages were measured once in August 2001, and again in April 2002 and July 2002, and the baseline leakages show excellent agreement between all three epochs. The higher s/n antenna-based leakages show similarly good agreement between August 2001 and April 2002, with residuals at all frequencies $\lesssim 1\%$, with the exception of three receivers. The polarizers for these receivers were retuned during the 2001 – 2002 austral summer, and systematic offsets can clearly be seen in the antenna-based residuals between these two epochs, the largest being approximately 2.5% in amplitude. Residuals between the April 2002 and July 2002 leakages are $\lesssim 1\%$ at all frequencies. Variations in the leakages of this magnitude are expected to have a negligible impact on the analysis presented in Paper V.

As discussed above, the parallactic angle modulation can be used to eliminate the leakage and place a limit on the intrinsic source polarization. Averaging over the

three epochs at which the leakages were measured, it is found that the polarization amplitude of RCW38, $P = (S_Q^2 + S_U^2)^{1/2}$, is less than 0.09% (of S_I) at all frequencies.

2.7.2. Off-Axis Leakage

Although the polarizers were optimized to yield low leakage, the lensed feed horns themselves will induce an instrumental polarization that varies across the primary beam. The instrumental polarization of the circularly symmetric lenses and feeds is expected to be azimuthally symmetric and depend only on the angle from the phase center.

To probe the off-axis response of the feeds, observations of RCW38 were made with the source at 16 offset positions in a 2.5° radius ring. The direction of the instrumental leakage is shown in the left panel of Figure 4. Within the measurement uncertainty this data is consistent with a simple radial pattern. In terms of S_Q and S_U , a radial pattern produces a quadrupole asymmetry across the primary beam, with the S_Q and S_U patterns rotated by 45° with respect to one another.

The radial amplitude profile of this off-axis leakage was characterized by observations of RCW38 and the Moon at various offsets (see Figure 4). The Moon data have extremely high s/n, permitting a separation of the data into several frequency bands. Attempts to model the off-axis leakage data as a simple perturbation of the aperture field reproduce the general shape and frequency dependence of the measured profile, but fail to replicate the sharp rise in amplitude seen between 1° and 2° . We therefore fit an empirical model by spline interpolation of the Moon data for the 29 – 33 GHz band (together with a point from RCW38 at 0.9° offset). The effect is assumed to scale with frequency in the same manner as the aperture field, and indeed this is supported by the Moon data at other frequencies. Additionally, the beam-offset RCW38 data confirms the validity of the model, agreeing within the measurement uncertainty.

The presence of off-axis leakage will transform CMB power from S_I into S_Q and S_U , and will bias the esti-

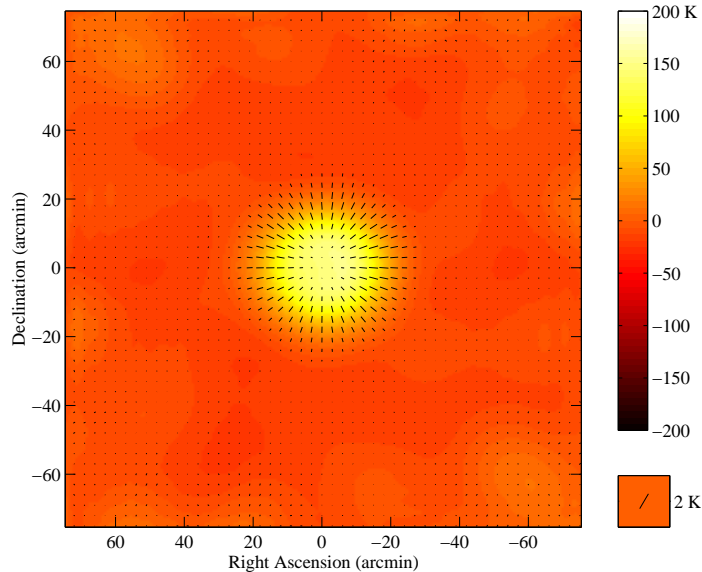


FIG. 5.— DASI image of the Moon. Shown is the total intensity map (greyscale), with measured polarization vectors overlaid, demonstrating the expected radial polarization pattern. These maps are dirty maps (see text) with $\sim 22'$ resolution, and the conversion to temperature units is therefore only approximate.

mation of polarization parameters from the data. These effects were investigated via extensive Monte Carlo simulation using the off-axis leakage model shown in Figure 4. As is shown in Paper V, the resulting bias on the various likelihood results presented in that paper is $\lesssim 4\%$ if the off-axis leakage is not accounted for in the analysis. Including our model of the off-axis leakage in the analysis, we can eliminate the bias to 1% or better.

Off-axis leakage will also transform power from point sources in the anisotropy fields into a polarization signal. In Paper V, we discuss the results of extensive simulations of this effect using the best available point source counts at cm-wavelengths. The results indicate that the bias on the derived CMB parameters is again small, of order a few percent or less.

3. POLARIZATION OBSERVATIONS WITH DASI

During the course of the 2001 – 2002 CMB observations, considerable effort was expended to characterize the polarization response of the instrument through observations of astronomical sources. In the preceding sections, we have described at length observations of the unpolarized HII region RCW38, on which the bulk of DASI’s calibration is based. Here we present polarimetric observations of a variety of other sources which provide independent checks of those calibrations, and lend confidence that we understand the various aspects of the instrumental response to a level (precision better than 1%) beyond that required to measure polarization in the CMB.

3.1. Observations of the Moon

At centimeter wavelengths, radiation from the Moon is dominated by thermal emission from the regolith, typically from the first $\sim 10 - 20$ cm of the Moon’s surface. This radiation is intrinsically unpolarized, but scattering off the dielectric discontinuity at the surface will induce

polarization; the tangentially polarized component is preferentially reflected, leading to a net radial polarization pattern across the disk of the Moon. This polarization amplitude decreases to zero at the center and increases to a maximum at the limb (see Moffat (1972) for a comparable result at 21 cm, and Mitchell & De Pater (1994) for a similar discussion and map of the microwave polarization of Mercury).

Observations of the Moon were made with DASI during 2001 – 2002 at several epochs, and at various phases of the Moon. All show excellent agreement with the expected radial polarization pattern, and the consistency between epochs attests to the stability of the absolute phase offset. In Figure 5 we present a polarized map of the Moon made during 21 – 22 August 2001, when the Moon was nearly full. These data have been corrected for instrumental leakages and the absolute phase offset determined from wire grid observations, discussed in §2.6.

Note that any residual phase offset in the cross-polar visibilities will introduce a vorticity to the polarization vectors, from which we can derive an independent measure of the cross-polar phase offsets. These measurements are shown in Figure 3, and are in excellent agreement with the phase offsets determined from the wire grid observations discussed in §2.6.

3.2. Observations of Galactic Sources

3.2.1. NGC 6334

Polarimetric observations of the Galactic source NGC 6334 were made in August 2001, centered on R.A. = $17^{\text{h}}20^{\text{m}}$, Dec. = $-35^{\circ}50'$ (J2000). NGC 6334 is a massive molecular ridge, with numerous embedded photodissociation regions, exhibiting the rich phenomenology typical of massive star-forming complexes. At radio and infrared wavelengths, emission from this complex encompasses a broad variety of phases of the interstellar medium, ranging from line and continuum emission from molecular

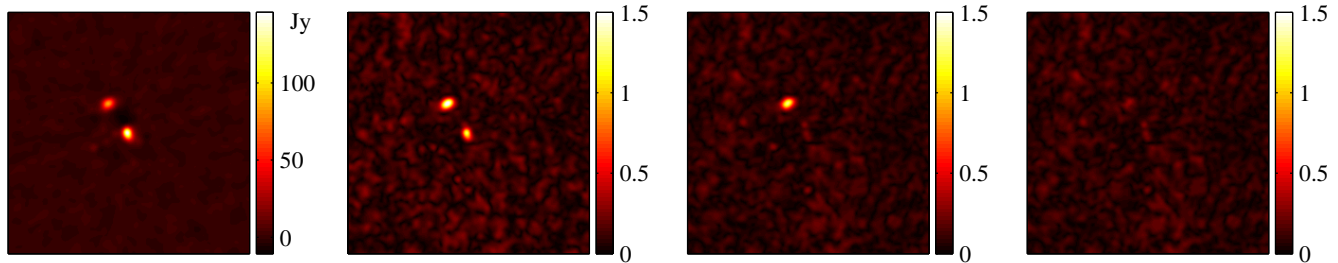


FIG. 6.— Observations of the molecular cloud complex NGC 6334. (left panel) Total intensity map. (center left) Map of $P = (S_Q^2 + S_U^2)^{1/2}$, uncorrected for leakage, showing structure correlated with the total intensity map, and at a level consistent with instrumental polarization. (center right) Map of P corrected for on-axis leakage. The central source has disappeared, and the on-axis residuals are consistent with intrinsic source polarization $< 0.14\%$. (right panel) Map of P , corrected for off-axis leakage, using the profiles shown in Figure 4. Fields are $12''.8$ across, with R.A. increasing to the left. All intensity scales are in Jy.

gas and dust, to optically thick and dust-obscured free-free emission from ionized gas in embedded HII regions (see for example Burton (2000), and Jackson & Kraemer (1999)).

In Figure 6, we present maps of the source in total intensity and polarization fraction. Artifacts of the Fourier sampling of the array have been reduced in these maps by an application of the CLEAN algorithm (Högbom 1974). At DASI’s $\sim 22'$ resolution, the microwave emission from the ridge is concentrated in two regions of comparable flux, one on-center, the second near the half-power point of the primary beam. This source therefore provides an ideal testbed for the leakage corrections described in §2.7.1 and §2.7.2. As can be seen in the second panel of Figure 6, the S_Q and S_U maps show emission coincident with these regions, at a level consistent with the instrumental leakages. Application of the on-axis leakage correction to the visibilities completely removes the central source in the polarization map, demonstrating that we can correct for instrumental leakage to better than 0.2%. Applying the off-axis leakage profile in the image plane similarly accounts for the second source.

The residuals after correction are consistent with the noise in the polarization map, indicating that the net polarization fraction from the variety of emission processes represented in the source is $< 0.14\%$.

3.2.2. Vela

As an application of the various calibrations discussed above, and a direct demonstration of DASI’s ability to map complex wide-field polarized emission, we present observations of the Vela supernova remnant. Inspection of the Parkes 2.4 GHz polarization maps (Duncan et al. 1997) shows that the Vela complex is an exceptional region, both for its size and intensity, and for its high fractional polarization ($\sim 30\%$). Observations were made of a field centered at R.A. = $08^{\text{h}}35^{\text{m}}$, Dec. = $-45^{\circ}46'$ (J2000).

The left and center right panels of Figure 7 show the resulting maps. Artifacts of the Fourier sampling have not been deconvolved from the map, i.e., these are “dirty” maps. In addition, we produced simulated DASI visibilities from the 2.4 GHz maps and made dirty maps from these with the same weightings as for the DASI data. The two sets of maps are therefore directly comparable, and within the limitations of noise will be the same in as much as the distribution of 26 – 36 GHz emission tracks that at 2.4 GHz. The 2.4 GHz maps are shown in the center left and far right panels of Figure 7.

As can be seen in the polarization maps, the 2.4 GHz vectors appear systematically rotated with respect to the 26 – 36 GHz vectors. A histogram of the difference between the polarization vector angles, weighted by the polarization amplitude, shows a clear peak at $+1$ rad. In the absence of a phase wrap, this implies a rotation measure of $\sim +70$ rad m^{-2} which is of the same order of magnitude as nearby line of sight measurements (Simard-Normandin, Kronberg, & Button 1981).

4. CMB OBSERVATIONS

4.1. Field Selection

For the total intensity anisotropy measurements presented in Paper I, we observed 4 rows of 8 fields separated by 1 h in right ascension. The locations of these fields were chosen as a compromise between observing at high elevation to minimize ground signal, and in regions showing very low levels of Galactic emission in both the IRAS 100 micron and Haslam 408 MHz maps (Haslam et al. 1981). We were able clearly to identify point sources from our own data within these fields as described in Paper I.

For the polarization observations presented here, we selected the C2 and C3 fields centered at R.A. = $23^{\text{h}}30^{\text{m}}$ and $00^{\text{h}}30^{\text{m}}$, and Dec. = -55° , within which no point sources had been detected. These fields lie at Galactic latitude $-58^{\circ}.4$ and $-61^{\circ}.9$, respectively. The brightness of the IRAS 100 micron and 408 MHz maps within our fields lie at the 6% and 25% points respectively of the integral distributions taken over the whole sky.

4.2. Observations

The fields were tracked over the full azimuth range in two-hour blocks. In any block, each field was tracked for approximately 1 hour over the same azimuth range, allowing a constraint on any residual ground signal not removed by the shields. Observations were divided into self-contained 24-hour segments. Each segment comprised 20 hours of CMB observation, and bracketing observations of the primary calibrator source RCW38. This source has been described at length in Paper I, and the reader is referred to that paper for details.

During 2000, observations of RCW38 performed every 12 hours demonstrated that instrumental gains were stable at the $\sim 1\%$ level over many days; during 2001 – 2002, the source was therefore observed only at the beginning and

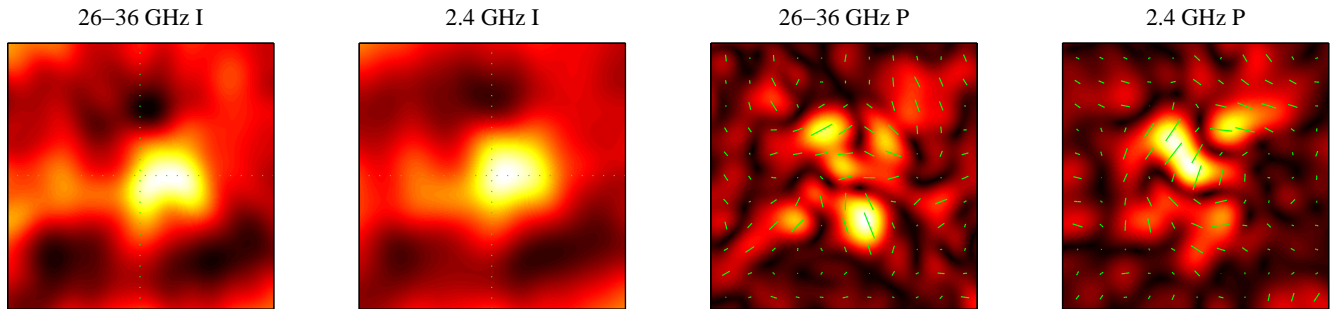


FIG. 7.— “Dirty maps” of the Vela region from DASI and as constructed from the Parkes 2.4 GHz survey (Duncan et al. 1997) with equivalent spatial filtering applied. (left pair) Color scale shows total intensity for the two cases. (right pair) Color scale shows polarized intensity ($P = (S_Q^2 + S_U^2)^{1/2}$) with vectors showing the electric field direction (length of vectors is proportional to P). Each map is 3° square.

end of the 20-hour CMB observations. In each calibrator scan, the source was observed for 35 minutes in each of the RR and LL configurations, from which the instrumental gains were determined for both the co-polar and cross-polar visibilities, as discussed in §2.5. In 35 minutes, we achieve an accuracy of $\lesssim 2\%$ on both the co-polar and cross-polar visibilities.

These observations were bracketed by skydips from which the opacity was determined, and by injection of a noise source used to calibrate the complex correlator, as described in Paper I.

To provide an additional level of consistency checks, observations were performed at two distinct rotations of the array faceplate (see §2), separated by 60° . Each 24-hour segment was observed at a fixed faceplate position, but the faceplate position was alternated roughly every day, so that approximately half the data from 2001 – 2002 were acquired in each orientation.

Fields were observed from 2001 April 10 to 2001 October 27, and again from 2002 February 14 to 2002 July 11. In all, 271 days of usable CMB data were acquired, 162 from 2001, and 109 from 2002, with the bulk of the remaining time spent on the observations described in §2.6–§3.2.2, as well as periodic observations to determine the pointing model of the telescope. As discussed in §2.7.1, observations to determine the on-axis leakages were repeated at three epochs to check the stability of the instrumental polarization. Observations to determine the cross-polar phase offset discussed in §2.6 were repeated twice to check for stability. Likewise observations of the Moon were repeated on three separate occasions during this time period.

4.3. Data Reduction

As described in Paper I, raw visibility data from the correlators are accumulated in 8.4-s integrations, along with monitoring data from various hardware systems throughout the telescope. After editing and calibration, the raw visibilities for each 24-hour period are combined, and these daily averages are the inputs to the analysis presented in Paper V. Edits applied to the data can be broadly divided into hardware and calibration edits applied to the raw integrations, and edits applied to the 24-hour averages, and we describe each of these in turn.

4.3.1. Calibration and Raw Visibility Cuts

As the first level of editing, the 8.4-s integrations are rejected during periods when a receiver LO was out of lock,

when a receiver was warm, or when the total power for a given receiver was outside the normal range. These cuts collectively reject $\sim 11\%$ of the data.

The only cut based on the visibility data values corresponds to a $> 30\sigma$ outlier rejection, to remove rare hardware glitches; this cut rejects $< 0.1\%$ of the data.

The surviving 8.4-s integrations from each 24-hour period are then calibrated for the relative amplitude and phase of the complex multipliers on the correlator cards, determined by the periodic injection of a broad-band noise source. These calibration factors have proved to be extremely repeatable in the three years that the telescope has operated, but we nevertheless reject baselines for which these factors lie on the tails of their distributions, indicating possible problems with the multiplier hardware. Data are rejected when the relative gain of the real and imaginary multipliers falls outside the range 0.6 – 1.2, or when the relative phase exceeds $\pm 20^\circ$, regimes for which the distributions of these factors over all baselines have become noticeably non-Gaussian. These cuts reject an additional 13% of the data.

As described in §2.4, every baseline samples the four Stokes states on a Walsh sequence. The observations presented here employ a period-16 Walsh sequence with a time step of 200 seconds, so that an observation is nominally completed in 3200 seconds. With the inclusion of switching time for the polarizers, however, the net observing time is somewhat less, and a reduction of > 200 s is generally an indication of a polarizer sticking (see the discussion of the polarizer assembly in §2.1). In combination with the cuts above, we therefore reject any scan with total time in a valid Stokes state < 3000 s, rejecting 0.1% of the data. Calibrator scans are also rejected if previous edits have reduced the total integration time by more than a factor of two. Loss of a calibrator scan results in the rejection of an entire day of data.

The data are next calibrated to remove complex instrumental gains, and to convert to absolute flux scale, using the bracketing observations of RCW38. This gain calibration is equivalent to the combination of the amplitude and phase calibration described in Paper I, but here we construct the cross-polar gains from antenna-based fits to the co-polar visibilities, as described in §2.5. The flux scale of RCW38 has been previously determined to 3.5% from measurements of absolute loads transferred to the source in 2000 and 2001, as discussed in Paper I.

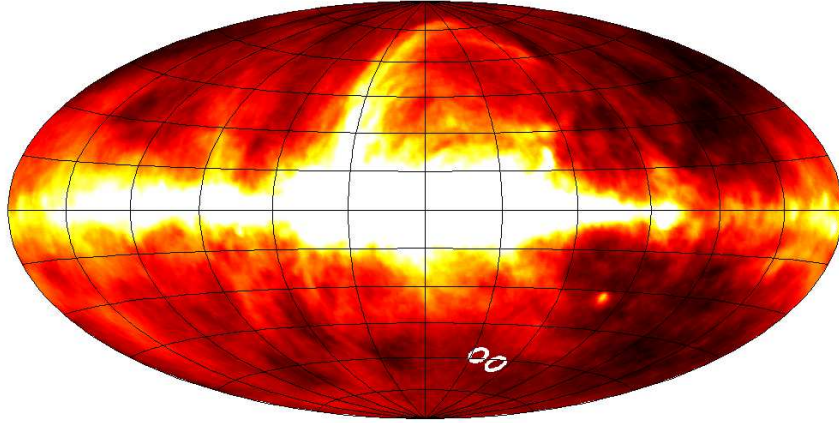


FIG. 8.— The 408 MHz synchrotron map (Haslam et al. 1981) with the location of the DASI polarization fields marked by white circles. The color scale is linear and has been clipped at one tenth of the maximum to allow the structure at high Galactic latitudes to be seen.

All data which lack bracketing calibrator scans are rejected, as are co-polar data for which the calibrator amplitude varies by $> 10\%$ over 24 hours, or for which the calibrator phase varies by $> 15^\circ$. For the cross-polar data, these limits are relaxed to 15% and 20° , as the lower s/n cross-polar data are dominated by thermal noise, and are therefore relatively insensitive to random errors in the daily calibration. These cuts reject 5% of the data.

4.3.2. Calibrated Visibility Cuts

After the raw data are edited and calibrated, the 8.4-s integrations are combined to form 24-hour averages of the visibilities for every baseline. (Recall that for a coplanar array, the projected baseline lengths do not change as a source is tracked across the sky, and that sources at the South Pole do not rotate in parallactic angle. The combination of visibilities on arbitrary timescales therefore engenders no loss of information due to smearing in the Fourier plane.) Cuts applied to the 24-hour averages include astronomical cuts (based on the position of the Sun and Moon), weather cuts, and cuts derived from the visibility noise.

In the first category, co-polar visibilities are cut whenever the Sun was above the horizon. The cross-polar visibilities show little evidence for contamination from the Sun at low elevations, and are rejected only when the Sun elevation exceeds $> 5^\circ$, or the Sun is closer than 90° to the fields and above the horizon.

The Moon rises and sets once a month at the Pole, and passes within 45° of the CMB fields. Although the data show little evidence of contamination for Moon elevations $< 10^\circ$, co-polar data were rejected when the Moon was above the horizon and closer than 80° and 60° , respectively, to the CMB and calibrator positions. A less stringent cut is imposed on the cross-polar data, as they are dominated by thermal noise and are therefore less sensitive to daily calibration uncertainties. For the 2002 data, there is evidence that the sunshield may actually increase the data scatter through secondary reflections when the Moon would otherwise be below the ground shield, and the 2002 co-polar data are rejected whenever the Moon is above the horizon.

The correlation matrix of visibilities was computed for

each day of data, over all 78 complex baselines, 10 correlator frequencies, and 4 Stokes states, where concurrent data from different Stokes states are available (see §2.4). This 6240×6240 matrix is inspected for off-diagonal correlations, and we reject entire days when the significance of any correlation exceeds 8σ , presumably due to weather. This cut rejects 22 days of data not already rejected by the lunar and solar cuts (8.1% of the data).

As an additional test of the correlator hardware, we form the sum of visibilities over consecutive pairs of 1-h observations, averaged over 24 hours, and over all baselines for each of DASI's 10 correlators. (Note, each correlator performs the 78 real and imaginary correlations for one of the ten 1 GHz-wide DASI frequency bands (see Padin et al. 2001, and Paper I).) This quantity is sensitive to output of the correlator that is coherent between observations of the two CMB fields. All data are rejected for an entire correlator on days when there is evidence for offsets large compared to the thermal noise. Not surprisingly, this statistic rejects data for all correlators taken during sunset 2002, but also rejects data from a single correlator which showed unusually large offsets throughout much of 2002. Of the data not previously rejected from the astronomical and weather cuts described above, this edit rejects an additional 1.9%.

Data are also rejected from an entire correlator on days when the 1-hour variance, averaged over all baselines of that correlator, is grossly discrepant with the mean variance over 2001 – 2002. Data are rejected on a per-baseline basis if the variance within any 1-hour period falls on the extreme tails of the expected reduced χ^2 distribution. Collectively, these edits reject a negligible fraction of the data.

For all of the cuts described above, the results are insensitive to small variations in the chosen cut levels. As discussed in Paper V, as these cut levels are varied, evidence for residual contamination eventually appears first in χ^2 consistency tests on differenced data sets, then as excess noise in the 1-hour observations, and only lastly in the likelihood results. The likelihood results are found to be insensitive even to quite large variations in the precise edit thresholds, and we are confident that the threshold settings introduce no significant bias in the CMB analysis.

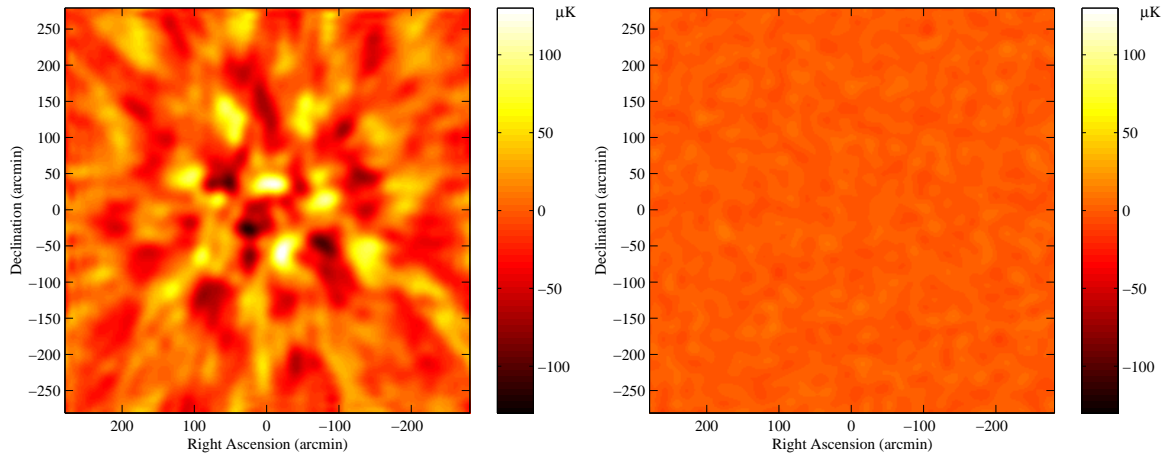


FIG. 9.— Total intensity maps of the differenced (C2–C3) CMB fields. (left panel) Sum map of two epochs containing equal amounts of data. (right panel) Difference map of the two epochs, plotted to the same temperature scale. The noise level in the map is $2.8 \mu\text{K}$, for a s/n at beam center of ~ 25 .

4.4. CMB Maps and Discussion

In this experiment, two CMB fields were observed to provide a constraint on any common signal not removed by the ground shield; accordingly, the analysis presented in Paper V pertain to the *differenced* visibilities of the two CMB fields. As described in that paper, the differenced visibilities are subjected to numerous consistency tests and no evidence is found for excess noise in any of the various subdivisions of the data by epoch, deck rotation or as a function of baseline length.

Shown in Figure 9 are total intensity maps of the differenced visibilities, where the maps are the sum and difference of two epochs with equal amounts of data. The sum map clearly shows structure enveloped by the primary beam of the feed horns, and as expected from the consistency tests, no residual signal is seen in the difference map above the noise. The detected structure is consistent with visibilities measured for these fields in the 2000 data presented in Paper I. With a noise floor in the difference map of $2.8 \mu\text{K}$, we achieve a s/n ratio of approximately 25 at beam center, for a synthesized beam of $\sim 22'$.

In Paper I, we gave estimates of the total intensity of synchrotron, free-free and thermal dust emission in the region of our fields, showing that the expected amplitudes are very small. This was confirmed in Paper II by template-based cross-correlation analysis which showed that the contribution of each of these foregrounds to our temperature anisotropy data is negligible.

The expected fractional polarization of the CMB is of order 10%, while the corresponding number for free-free emission is less than 1%. Diffuse thermal dust emission may be polarized at the several percent level see, e.g., Hildebrand et al. (2000), although the admixture of dust and free-free emission observed with DASI in NGC 6334 is $\ll 1\%$ (see §3.2.1, and Figure 6). Likewise, emission from spinning dust is not expected to be polarized at detectable levels (Lazarian & Prunet 2002). Therefore if free-free and dust emission do not contribute significantly to the temperature anisotropy results they are not expected to contribute to the polarization.

As described in §4.1, no point sources are detected in

either field, and there is at best scant evidence for a correlation between the locations of the 31 brightest PMN sources and the pixel values in the map. Nevertheless these sources, whose 5 GHz flux when enveloped with the DASI primary beam exceeds 50 mJy, are projected out of the co-polar data for all of the likelihood results presented in Paper V.

As discussed in Paper V, with these sources projected out of the differenced co-polar data, the temperature spectral index is consistent with a thermal spectrum ($\beta = -0.01 \pm 0.15$, where $T \propto \nu^\beta$). Any significant non-thermal emission can be excluded with high confidence. If none of the PMN sources are projected out, the spectral index limit shifts to -0.12 ± 0.13 , indicating that the PMN sources may be detected statistically, but that the CMB is nevertheless the dominant signal in these fields. With no PMN sources projected out of the cross-polar data, the spectral index of the polarized visibilities is also consistent with a thermal spectrum, though with considerably lower s/n $\beta = 0.17 \pm 1.8$ (68% confidence). Though this result alone is not conclusive, we note that it is inconsistent with synchrotron at nearly the 2σ level.

5. CONCLUSION

We have described an experiment to measure polarization in the CMB, using the Degree Angular Scale Interferometer (DASI). New broadband polarizers were installed in the telescope in 2001, and careful optimization of these polarizers prior to installation resulted in achromatic performance across DASI's frequency band to $\lesssim 1\%$, as confirmed by astronomical observations. We have developed techniques which allow us to calibrate the polarimeter end-to-end using only unpolarized sources, and an extensive campaign of observation has resulted in a characterization of the instrumental polarization response to levels well below what is required for a detection of CMB polarization. Observations of the Moon and various Galactic sources demonstrate that DASI can map degree-scale polarization to high accuracy.

During 2001 – 2002, the telescope acquired 271 days of data in all four Stokes parameters on two fields identified

from previous observations with DASI as containing no detectable point sources. The data show no evidence for contamination by point sources, polarized or unpolarized, and both the total intensity and polarization data are consistent with a thermal spectrum. These observations show structure from the CMB detected with an unprecedented s/n of ~ 25 .

We are indebted to the Caltech CBI team led by Tony Readhead, in particular to Steve Padin for a considerable fraction of DASI's electronics design, to John Cartwright for the downconverter design and to Martin Shepherd for data acquisition software. We thank Raytheon Polar Services for their support of the DASI project, including the erection of the DASI ground shields, and in particular Roger Rowatt and his crew. We are indebted to the Center for Astrophysical Research in Antarctica (CARA), in particular the efforts of Allan Day, Stephan Meyer, Nancy Odalen, Bob, Dave and Ed Pernic, Bob Lowenstein, Bob Spotz, Michael Whitehead and the CARA polar opera-

tions staff. We thank Jacob Kooi for his assistance with the installation of the polarization hardware, John Yamasaki for help with electronics, Ellen LaRue and Gene Drag for the assembly of the calibration wire grids, Mike Loh for assistance with the sunshield and Kim Coble for analysis of DASI primary beam measurements. We thank the TopHat collaboration for the use of their sun shield. We thank the observatory staff of the Australia Telescope Compact Array, in particular Bob Sault and Ravi Subrahmanyam, for their generosity in providing point source observations of the DASI fields. This research was initially supported by the National Science Foundation (NSF) under a cooperative agreement (OPP 89-20223) with CARA, a NSF Science and Technology Center; it is currently supported by NSF grant OPP-0094541. JEC gratefully acknowledges support from the James S. McDonnell Foundation and the David and Lucile Packard Foundation. JEC and CP gratefully acknowledge support from the Center for Cosmological Physics.

REFERENCES

- Burton, M. G. e. a. 2000, *ApJ*, 542, 359
 Duncan, A. R., Haynes, R. F., Jones, K. L., et al., 1997, *MNRAS*, 291, 279
 Halverson, N. W., Leitch, E. M., Pryke, C., et al., 2002, *ApJ*, 568, 38
 Haslam, C. G. T., Klein, U., Salter, C. J., et al., 1981, *A&A*, 100, 209
 Hildebrand, R. H., Davidson, J. A., Dotson, J. L., et al., 2000, *PASP*, 112, 1215
 Högbom, J. A. 1974, *A&AS*, 15, 417
 Hu, W. & White, M. 1997, *New Astron.*, 2, 323, astro-ph/9706147
 Jackson, J. M. & Kraemer, K. E. 1999, *ApJ*, 512, 260
 Kamionkowski, M., Kosowsky, A., & Stebbins, A. 1997, *Phys. Rev. D*, 55, 7368
 Kovac, J. M. & Carlstrom, J. E. 2002, *IEEE MTT*, in prep.
 Kovac, J. M., Leitch, E. M., Pryke, C., et al., 2002, *ApJ*, astro-ph/02
 Lazarian, A. & Prunet, S. 2002, in *AIP Conference Proceedings*, Vol. 609, "Astrophysical Polarized Backgrounds", ed. S. Cecchini, S. Cortiglioni, R. Sault, & C. Sbarra (Melville, NY: AIP), 32
 Leitch, E. M., Pryke, C., Halverson, N. W., et al., 2002, *ApJ*, 568, 28, astro-ph/0104488
 Mitchell, D. I. & De Pater, I. 1994, *Icarus*, 110, 2
 Moffat, P. H. 1972, *MNRAS*, 160, 139
 Padin, S., Cartwright, J. K., Shepherd, M. C., et al., 2001, *IEEE Trans. Instrum. Meas.*, 50, 1234
 Pryke, C., Halverson, N. W., Leitch, E. M., et al., 2002, *ApJ*, 568, 46
 Simard-Normandin, M., Kronberg, P. P., & Button, S. 1981, *ApJS*, 45, 97
 Zaldarriaga, M. & Seljak, U. 1997, *Phys. Rev. D*, 55, 1830